ADVANCED MATERIALS
www.advmat.de

Wideband Tuning and Deep-Tissue Spectral Detection of Indium Phosphide Nano-Laser Particles

*Sangyeon Cho, Wonjoon Moon, Nicola Martino, and Seok Hyun Yun**

Laser particles (LPs) emitting narrowband spectra across wide spectral ranges are highly promising for high-multiplex optical barcoding of biological cells. Here, LPs based on indium phosphide (InP) nanodisks are presented, operating in the near-infrared wavelength range of 740–970 nm. Utilizing low-order whispering gallery resonance modes in size-tuned nanodisks, an ultrawide color palette with 25% spectral utilization and nanometer-scale linewidth is achieved. A simple theoretical model accurately predicts spectral ranges based on particle size. The minimum laser size is 430 nm in air and 560 nm within cells, operating at mode orders of 4 or 5. The high brightness and narrow linewidths of polymer-silica-protected InP LPs, combined with a silicon-detector spectrometer, enable spectral detection of laser peaks with high signal-to-background ratios in highly-scattering media, including 1-cm-thick chicken breast tissue and blood vessels in live mice.

1. Introduction

Near-infrared (NIR) spectral ranges have gained increasing attention for expanding multiplexing capabilities beyond the conventional visible fluorescence spectrum and enabling deep tissue imaging.[1–3] In biological tissues, optical absorption decreases significantly at wavelengths above 750 nm, and light scattering also steadily declines with increasing wavelength.[4] This makes NIR light particularly advantageous for biological imaging. The NIR spectrum is typically divided into two subregions: NIR-I (750–1000 nm) and NIR-II (1000–1700 nm, also known as the short wavelength infrared or SWIR), with detection commonly achieved using silicon (Si) for NIR-I and indium-gallium-arsenide (InGaAs) photodetectors for NIR-II. Various types of NIR fluorophores have been developed, including fluorescent proteins,[5] single-walled carbon nanotubes,[6] quantum dots,[7] lanthanide-doped nanoparticles,[8] organic dyes, and polymers.[9] However, these conventional luminescent reagents typically exhibit emission linewidths of 50–200 nm in the NIR range, limiting their potential for applications requiring high spectral resolution.

Standalone micro- and nanoscale lasers, known as laser particles (LPs), have recently emerged as innovative optical emitters for biological applications. LPs generate much narrower linewidths (<1 nm) than traditional fluorophores, making them ideal for applications such as large-scale spectral barcoding[10–14] and spectral sensing.[15,16] These particles are typically fabricated from III-V semiconductor alloys in discoidal shapes, with optical resonances that can be precisely tuned by adjusting particle size. This design allowed LPs to achieve a wide emission range, spanning 30–50 nm with multi-quantum-well[11] or bulk semiconductors[13] in the far-red spectrum (650–730 nm) and 80–120 nm per alloy in the NIR II range.[10]

LPs with whispering gallery (WG) mode lasing can achieve wavelength-scale dimensions (e.g., 1.6–2 μm for NIR-II). While these sizes are too large for molecule-specific targeting, they are well-suited for large-scale cell barcoding and single-cell tracking analysis.[12] LP emission is exceptionally bright, equivalent to the output of over 10 000 fluorophores with a submicron volume, without concentration quenching or photobleaching. This high brightness, combined with narrowband emission, ensures strong signal-to-noise performance and effective rejection of spectrally broad background noise. These unique properties make LPs highly promising for cell barcoding and sensing applications within scattering tissues, live animals, and in vitro environments.

Here, we present LPs made from indium phosphide (InP) that operate within the NIR-I spectral range. While InP has been used for conventional diode and nanowire lasers,[17] its potential in free-standing LPs has remained unexplored until now. Our findings reveal that the high gain of InP enables low-order WG mode lasing, allowing ultrawide tunability of the lasing wavelength across different mode orders. By varying particle sizes from 450 to 1000 nm, we achieve a tunable emission range from 740 to 970 nm. A simple theoretical model of WG lasers is introduced to explain the observed tuning behavior based on particle size. Leveraging the high output intensity and background noise rejection of these LPs, we demonstrate their effective detection within cells, thick tissues, and blood stream in live mice.

S. Cho, W. Moon, N. Martino, S. H. Yun
Harvard Medical School and Wellman Center for Photomedicine
Massachusetts General Hospital
Cambridge, Massachusetts 02139, USA
E-mail: syun@hms.harvard.edu
S. H. Yun
Harvard-MIT Health Sciences and Technology
Massachusetts Institute of Technology
Cambridge, Massachusetts 02139, USA

The ORCID identification number(s) for the author(s) of this article can be found under https://doi.org/10.1002/adma.202418710

DOI: 10.1002/adma.202418710

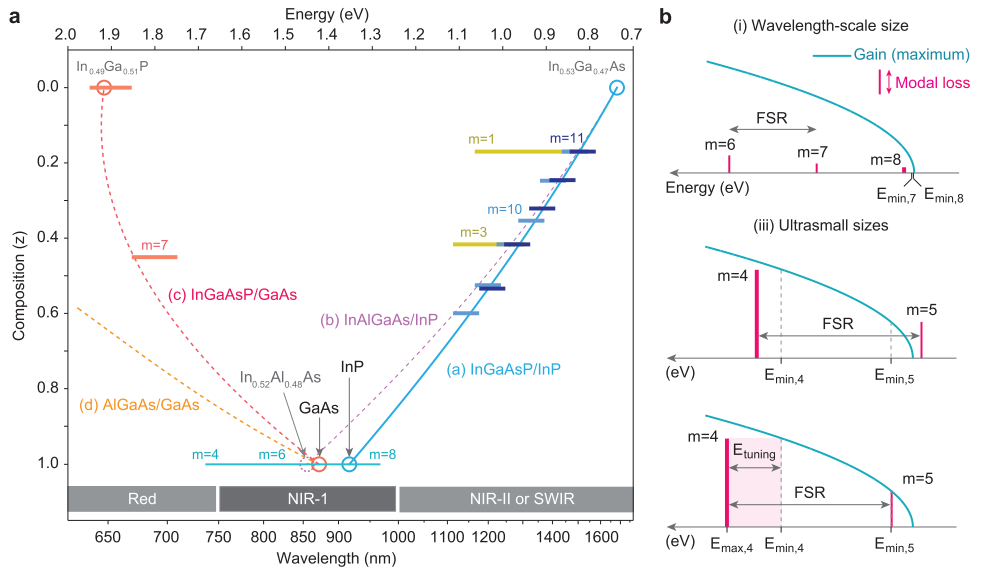

Figure 1. Bulk semiconductor material options for NIR-I LPs. a) Stoichiometry trajectories of band gap energy for four major III-V alloys: (i) InGaAs/InP: $(In_{0.53}Ga_{0.47}As)_z(InP)_{1-z}$, (ii) InAlGaAs/InP: $(In_{0.53}Ga_{0.47}As)_{1-z}(In_{0.52}Al_{0.48}As)_z$, (iii) InGaAsP/GaAs: $(In_{0.49}Ga_{0.51}P)_{1-z}(GaAs)_z$ and (iv) $(AlAs)_{1-z}(GaAs)_z$. Horizontal bars represent experimentally observed spectral ranges from earlier works: ref. [10]: dark blue, ref. [12]: blue, ref. [14]: yellow, and ref. [13]: orange. The thin blue-green line at z = 0 represents this work. b) Illustration of the relationship between lasing mode order and device size for a given semiconductor. Solid blue curves represent the maximum gain, which is proportional to the density of states. For each case, the lasing mode corresponds to the lowest-order mode that satisfies $E_p > E_{min}$: (i) $m = 10$ and (ii) $m = 4$. The insets show the theoretical profiles of the z-component of the magnetic field (Hz) for the lasing transverse electric modes in two different disk sizes: (i) $2R = 1200$ nm and (ii) $2R = 600$ nm. The tuning range E_{tuning} for the m-order mode is given by the difference between $E_{min,m+1} + E_{FSR}$ and $E_{min,m}$, indicated by the shaded light red region.

2. Results

2.1. Semiconductor Material Options in the NIR-I Range

For the NIR-I range (750–1000 nm), four bulk III-V semiconductor options exist: InGaAsP alloys lattice-matched to InP substrates, InAlGaAs latticed-matched to InP substrates, and InGaAsP lattice-matched to GaAs substrates.[18] **Figure 1a** depicts the band gap energy of these alloys as a function of compositional parameter (see Figure caption), along with experimentally demonstrated spectral ranges with micro- and nano-disks made of each of these materials. Interestingly, all four stoichiometry trajectories converge within a narrow wavelength range of 860 to 920 nm. Therefore, materials such as InP, $In_{0.52}Al_{0.48}As$, and GaAs, or their closely related quaternary compositions, are suitable options for NIR-I LPs. In this work, we selected InP due to its lower surface recombination rates compared to GaAs, resulting in reduced surface defects.[19] Additionally, unlike InAlAs, InP does not contain aluminum, which is prone to oxidation in water.[20]

From laser disks with random, wavelength-scale diameters, we have previously observed tuning ranges of approximately 50–100 meV around band gap energies. Consequently, we expected InP to cover a similar range in the NIR-I. Surprisingly, we found that InP supported lasing with subwavelength disk diameters, extending the tuning range beyond 0.4 eV (Figure 1a).

To describe the tuning range in more detail, consider a semiconductor disk with a radius R and an effective modal refractive index n. The resonance wavelength λ of a WG mode with mode order m is approximately given by

$$2\pi nR = \left(m + m_0\right)\lambda \tag{1}$$

where m_0 is an offset that accounts for the fact that the WG mode propagates along a path with an effective radius smaller than the physical disk radius. Rearranging Equation (1), we obtain $m = \frac{2\pi n}{\lambda}\left(R - \frac{m_0}{2\pi}\frac{\lambda}{n}\right)$. From this expression, it follows that $\frac{m_0}{2\pi}\frac{\lambda}{n}$ corresponds to the difference between the physical radius and the effective mode radius. Thus, m_0 quantifies this radial offset in terms of optical phase. For InP disks with low mode orders, we find that m_0 is less than π (Supplementary Note 1.) From (1), the corresponding photon energy is given by $E_p = \frac{hc}{2\pi nR}\left(m + m_0\right)$, where h is Planck's constant and c is the speed of light. The energy separation between adjacent modes, known as the free spectral range (FSR), is given by

$$\Delta E_{FSR} = \frac{hc}{2\pi nR} = \frac{E_p}{\left(m + m_0\right)} \tag{2}$$

For the m-order mode to be the lasing mode, it must satisfy two conditions: First, the unsaturated optical gain must exceed the optical loss of the mode. In a bulk semiconductor, the density of states is proportional to $\sqrt{E_p - E_g}$, where E_g is the band gap energy. Consequently, the maximum gain coefficient can be expressed as $g = A\sqrt{E_p - E_g}$, where A is a material-dependent constant independent of photon energy. The loss coefficient can

be written in terms of the modal Q-factor (Q) as $\gamma = E_p/Q$. While pure radiative Q-factor increases exponentially with mode order, other loss mechanisms limit the overall modal Q. In practice, the Q-factor can be better approximated using a power law dependence: $Q \propto m^p$, where p is a constant. For small III-V disks with $Q < 1000$, $p \approx 3$ provides a good approximation. Using this, the loss coefficient becomes $\gamma = BE_p m^{-p}$, where B is a coefficient. The minimum photon energy satisfying the lasing condition $g \geq \gamma$ is then given by:

$$E_{min} = E_g + \left(\frac{B}{A}\right)^2 E_p^2 \frac{1}{m^{2p}} \tag{3}$$

The second condition requires that the next higher-order mode resonance has significantly lower gain (lying outside the bandgap edge), ensuring that the $(m + 1)$-order mode with lower cavity loss does not become the lasing mode. Once the higher-order mode reaches the lasing threshold, it depletes optical gain and frustrates the lasing of the lower-order modes. This situation is illustrated in Figure 1b. We find that the tuning range for a specific mode order cannot exceed the FSR. Wavelength-scale semiconductor LPs operate with mode orders between 8 and 11, yielding $\Delta E_{FSR} \approx 0.1\ E_p$. With sufficient gain available, the FSR-limited maximum photon energy the m-order lasing mode can achieve is:

$$E_{max} = \Delta E_{FSR} + E_{min,m+1} \tag{4}$$

where $E_{min,m+1}$ denotes E_{min} of the $(m + 1)$-order mode, where the higher mode can lase before the m-order mode. The tuning range, ΔE_{tuning}, of the m-order mode is then given by:

$$\Delta E_{tuning}(m) = E_{max}(m) - E_{min}(m) \tag{5}$$

The minimum mode order, m_{min}, that can achieve lasing is derived from the condition $\Delta E_{tuning} > 0$. As the mode order increases, E_{min} approaches E_g, and ΔE_{tuning} approaches E_{FSR}, decreasing inversely with the mode order. While the analysis above assumes the maximum achievable gain profile, in practice, the actual gain is often lower than the theoretical maximum due to factors such as limited pump energy and nonradiative carrier recombination. As a result, m_{min} is typically higher than that the value estimated from the condition $E_{max} = E_{min}$. When considering an ensemble of LPs lasing with all possible mode orders, the maximum spectral range, ΔE_{group}, is given by

$$\Delta E_{group} = E_{max}(m_{min}) - E_{min}(\infty) \tag{6}$$

The spectral utilization factor is defined as the ratio $\Delta E_{group}/E_p$.

At the edge of the tuning range, where two neighboring modes experience equal net gain, two-mode lasing can occur.[21] In much larger microbead lasers,[16,22] multimode lasing is commonly observed due to reduced mode spacing and smaller gain differences between adjacent modes. When multiple modes have comparable net gain, they may lase simultaneously or exhibit transient switching because of mode competition. In contrast, single-mode lasing is predominant in sub-wavelength-sized lasers.

2.2. Particle Fabrication and Lasing Characteristics

To fabricate InP nanodisks, we used a wafer that consists of four InP layers and three sacrificial InGaAsP layers grown on an InP substrate (**Figure 2**a, and Methods). The thickness of each InP layer was 340 nm. Initially, pillars with diameters ranging from 900 to 1100 nm were fabricated by optical lithography and reactive ion etching. Subsequent wet etching with a piranha acid solution (H_2SO_4:H_2O_2:H_2O = 1:1:10) removed the sacrificial layers, producing free-standing InP particles (Figure 2b). The particles were transferred onto a glass substrate and characterized with a home-built hyperspectral microscope. The setup employed a frequency-doubled Nd:YAG nanosecond laser (532 nm wavelength, 5 ns pulse width) and a picosecond laser (765 nm, 70 ps pulse width) for pumping, and electron-multiplying silicon cameras, time-correlated single photon counting hardware, and a diffraction grating-based spectrometer for output characterizations.

The light-in-light-out curve exhibited the expected threshold behavior with a spontaneous emission β-factor of 10^{-3} (Figure 2c). Below the threshold, the photoluminescence (PL) spectrum showed a broad spontaneous emission with a 38 nm width. Above a pump energy of 0.22 mJ cm^{-2}, calculated from an input pulse energy of 27 pJ focused to a spot size of 4 µm, a sharp single-mode laser peak emerged (Figure 2d). The linewidth was 0.2 nm at threshold (Figure 2e), beyond which the linewidth increased modestly at higher pump powers. Under picosecond pumping, the threshold pump energy remained approximately 0.2 mJ cm^{-2}, similar to nanosecond pumping, but the linewidth broadened to 0.55 nm. Following picosecond pumping, the decay time of the output decreased significantly above the lasing threshold (Figure 2f), as stimulated emission became dominant over spontaneous emission (Figure 2g). While the spontaneous emission decay time was approximately 1 ns, the stimulated emission decay time above the threshold was <120 ps, limited by the instrument temporal resolution. According to finite-difference time-domain (FDTD) numerical simulation, the lasing mode expected for a disk diameter of 900 nm is the seventh-order transverse-electric WG mode (Figure 2h), with a Q-factor of ~ 360 in air. This mode has the highest Q factor among several other modes within the gain bandwidth. Experimental Q factors may be lower due to surface roughness and shape imperfections. Wide-field imaging of InP particles showed the ring profiles (Figure 2i), expected for the WG mode (Figure 2j).

2.3. Ultrawide Tuning of Lasing Wavelength by Size

We initially prepared InP microdisks with diameters of 1000 ± 60 nm (batch v). To achieve size reduction, the harvested microdisks underwent additional wet etching in an 85% wt H_3PO_4 solution at 70 °C, with an etching rate of 17 nm/sec (34 nm/sec in diameter). By varying the etching time, we created additional batches with different mean sizes: 900 nm (batch iv), 730 nm (batch iii), 560 nm (batch ii), and 480 nm (batch i) (**Figure 3**a). The size variation within the original batch proportionally decreased with size reduction. The etching rate of InP is higher along the [001] and [010] planes compared to the [011] plane.[23] Due to this anisotropic etching, the shape of the disks transformed from

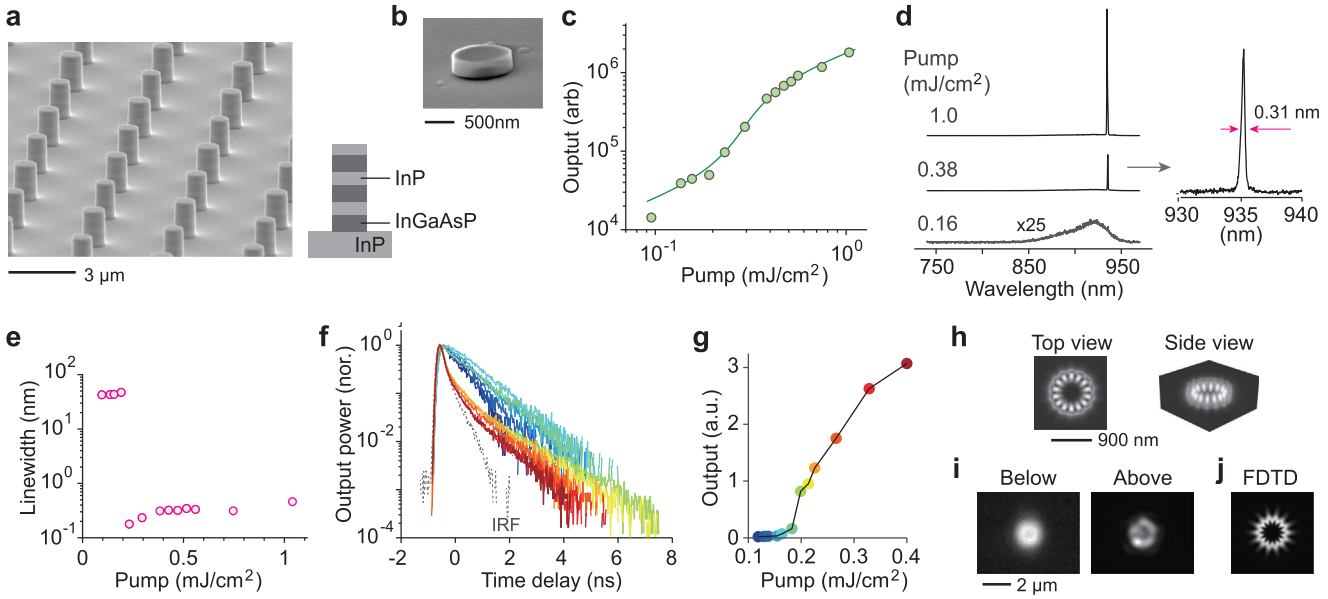

Figure 2. Output characteristics of InP disks. a) Scanning electron micrograph (SEM) of fabricated micropillar arrays on a wafer. Inset: wafer design. b) SEM of an isolated InP particle. c) Measured light-in-light-out curve. Dashed line: theoretical fit. d) (Left) Output spectra at different pump fluences: 0.16, 0.38, and 1 mJ cm^{-2}. (Right) A zoomed-in view of the spectrum at 380 μJ cm^{-2}. e) Measured output linewidth. f) Transient lifetime decay curves from InP particles with a mean diameter of 900 nm. Colors correspond to different pump powers, increasing from cyan to dark red. g) Light-in-light-out curve for the sample in (f), with the same color encoding for different pump levels. h) FDTD-simulated electric field amplitude, |E|, of the lasing mode with an azimuthal mode order of 7 at a wavelength of 940 nm. i) Measured far-field emission profiles below and above lasing threshold. j) FDTD simulation for the far-field profile of the lasing mode.

near-circular (batch v) to ellipsoid (batch iv) and eventually to cube-like shapes (batches i–iii).

Figure 3b presents the above-threshold spectra from a total 880 disks across the five batches. As the disk size decreased, the lasing wavelength gradually blue-shifted, reaching 740 nm for batch i. The longest observed wavelength was 970 nm in batch v. This resulted in a total tuning range of 230 nm (approximately 100 THz), corresponding to a frequency bandwidth utilization of 25%, calculated as the tuning range divided by the center frequency. The achieved tuning range is comparable to that of bulk Ti:Sapphire lasers, which are known for their exceptionally wide tunability. We note that, unlike conventional tunable lasers that typically employ narrowband spectral filters, wavelength selection in micro- and nano-LPs is governed by the relatively large separation of mode positions across a semiconductor level-filling gain profile (Figure 1b).

The mean lasing threshold energy was 150 μJ cm^{-2} for batch v and increased to 4 mJ cm^{-2} for batch i (Figure 3c). The linewidth also broadened from ≈0.3 nm in batches v-iii (Figure 3d) to 1.5 nm in batch i. The Q factor (Q) of the lasing mode, as calculated using FDTD simulations, decreased from ≈360 in batch v to 80 in batch i (Figure 3e). Almost all samples from batches i to v exhibited single modes across pump intensities ranging from 0.2 to 4 mJ cm^{-2} (Figure 3f). While particles from batches ii to v showed nearly negligible spontaneous emission, smaller particles from batch i exhibited a significant spontaneous emission background at 860–940 nm. Similar spontaneous emission has been observed in half-wave plasmonic lasers ($m = 1$) and attributed to the waterfall-like transitions of pump-generated carriers toward the bandgap edge.[14]

Lasing WG mode orders decreases progressively from batch v to batch i. The measured maximum photon energy (E_{max}) showed good agreement with Equation (4), where the mean mode order was calculated with $n = 2.7$ and $m_0 = \pi/4$ (Figure 3g). Equation (3) accurately describes the measured E_{min} with the best-fit parameters: $p = 3$, $(B/A)^2 E_g = 500$, and $E_g = 1.3$ eV (Figure 3g). The power-law parameter $p = 3$ is consistent with the Q-factor dependence (Figure 3e). The measured tuning range, $E_{max} - E_{min}$, is well explained by the theoretical model (Figure 3h,i). The Mie scattering diagram (Figure 3j) illustrates the tuning curves of different modes for different batch sizes. The azimuthal mode order decreases from 7–8 in batch v to order 4 in batch i in air.

For lasing to occur, the optical gain must exceed the cavity loss of the mode. The threshold gain coefficient can be approximated as $2\pi n/\lambda Q$. For a particle size of 480 nm, the required gain coefficient is ≈ 3400 cm^{-1}, whereas a larger particle size of 1000 nm requires only 740 cm^{-1}. Gain increases with pump fluences as more free electrons and holes are generated. Using a semiconductor model based on the Fermi-Dirac distribution of carriers,[24–26] we calculated the gain coefficients as a function of wavelength for different pump levels at room temperature. These are plotted in Figure 3k for carrier densities ranging from 10^{17} to 4×10^{19} cm^{-3}. As the pump fluence increases, free electrons and holes populate deeper into the conduction and valence bands, resulting in higher gain at shorter wavelengths. This phenomenon explains the observed blue-shift of the lasing wavelength in smaller particles. The gain profile is similar to spontaneous emission spectra. Figure 3l shows experimentally measured PL spectra from non-lasing, 200 nm-sized InP particles on a glass substrate at various pump fluences, approaching the

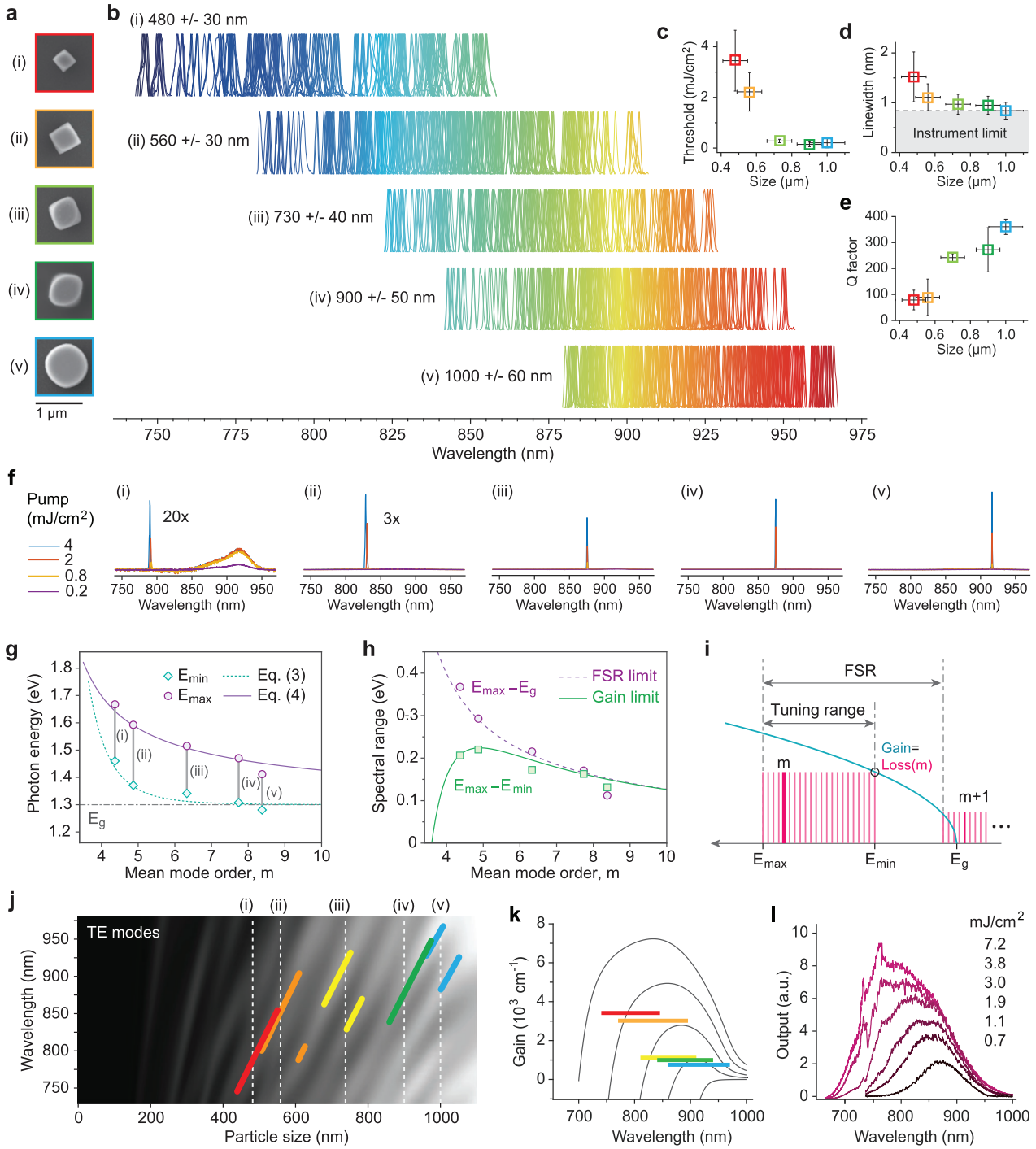

Figure 3. Size-dependent characteristics of InP LPs. a) SEM images of representative particles from different batches with different sizes: (i) 480 ± 30 nm, (ii) 560 ± 30 nm, (iii) 730 ± 40 nm. (iv) 900 ± 50 nm, and (v) 1000 ± 60 nm. b) Normalized emission spectra from numerous particles within each batch. c) Measured lasing thresholds for each batch. d) Measured lasing linewidths for each batch, with a spectrometer resolution of 0.8 nm. e) Calculated Q factors of the lasing modes. Data points in panels (c)–(e) are color-coded corresponding to their batches. f) Representative emission spectra of single particles from batches i to v at different pump intensities, ranging from 0.2 to 4 mJ cm^{-2}. g) Experimentally measured E_{min} and E_{max} and theoretical curves based on Equation (3) and (4) with $p = 3$, $m_0 = \pi/4$, and $(B/A)^2 E_g = 500$. h) Measured spectral range values and theoretical curves (Equation (5). i) Illustration of modal tuning range. j) Light scattering simulations illustrating the evolution of different transverse-electric (TE) WG modes as a function of particle size. Vertical dashed lines indicate the mean sizes of different batches, and thick color lines represent the expected tuning curves of the lasing modes within each batch. k) Simulated semiconductor gain spectra at room temperature for carrier densities of 0.1, 5, 10, 20, 40 × 10^{18} cm^{-3}. Horizontal color bars indicate the loss coefficients ($2\pi n/\lambda Q$) of the lasing modes and their spectral ranges for different batches. (l) Measured PL spectra from a non-lasing, 200 nm-sized InP particle under various pump fluences, illustrating the relationship between increasing gain coefficients and the blue-shift of the gain spectra.

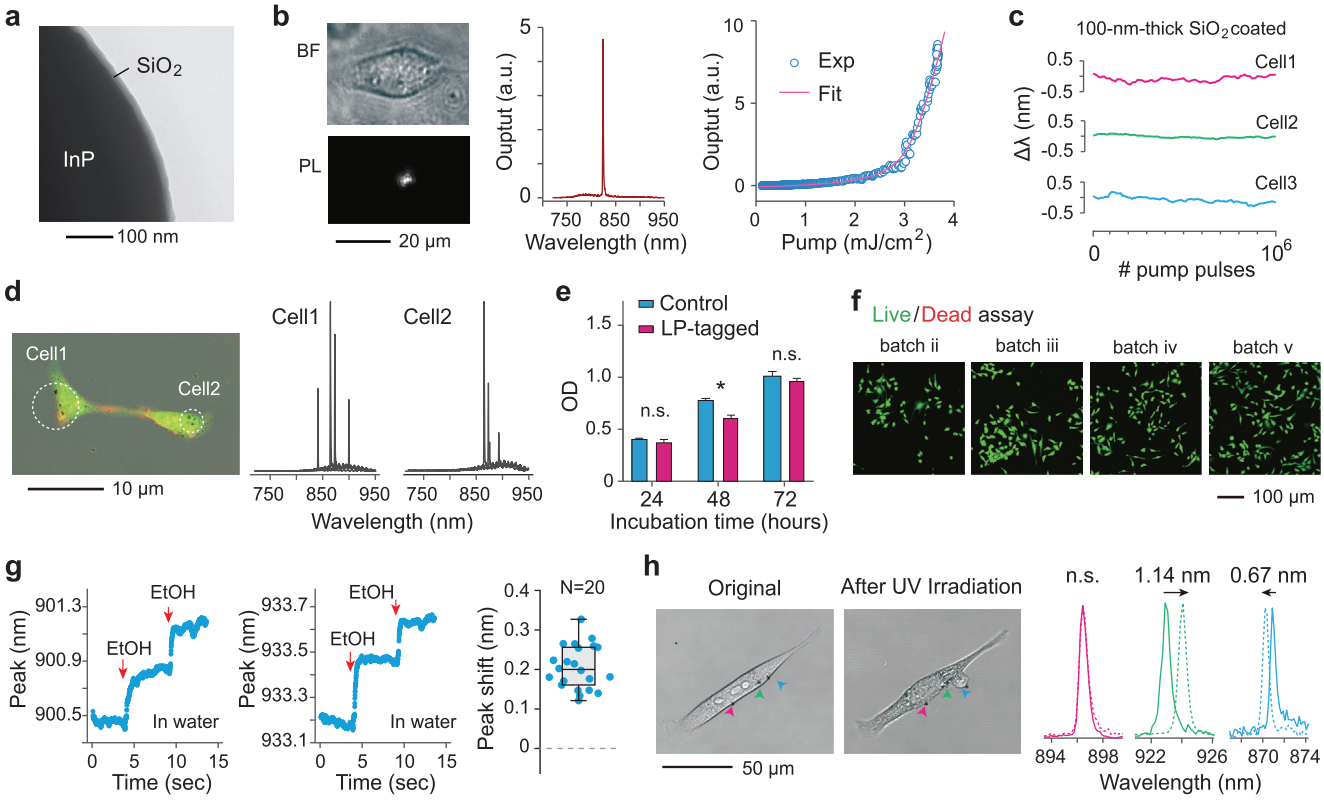

Figure 4. Laser characteristics within the cell. a) TEM image of an InP disk coated with a silica layer. b) (Left) Bright field (BF) and PL images of a 560 nm-sized LP within the cytoplasm of a live HeLa cell. (Middle) Output lasing spectrum. (Right) Light-in-light-out data. Solid curve: theoretical fit. c) Wavelength fluctuations of three InP LPs coated with a 100 nm-thick silica layer, immersed in water during active operation with 1 million pump pulses at 10 kHz. d) (Left) Fluorescence image of two HeLa cells (green cytoplasm dye, orange membrane dye), each tagged with four InP LPs. (Right) Output spectra from these cells. e) CCK assay result for LP-tagged cells (blue) and un-tagged control HeLa cells (red). n.s.: not significant; *$p < 0.001$. f) Live (green) and dead (red) assay images of LP-tagged cells from four different batches. g) Wavelength shifts of two InP LPs without silica coating in a reaction bath with 100 μL of water, following two sequential additions of 20 μL of ethanol (indicated by arrows). (Right) Data from twenty lasers, a median shift of 0.27 nm, with a standard deviation of 0.05 nm. h) (Left) BF images of a Hela cell before and after apoptosis induced by UV irradiation. Red arrow indicates an LP on the membrane, green indicates an LP near a rupture region, and cyan indicates an LP near a protruding membrane. (Right) Output spectra from these LPs before (solid curves) and after (dashed curves) the UV irradiation.

material damage threshold of ≈8 mJ cm^{-2}. Clear blue-shifts of the peak gain range are observed with increasing pump fluence, demonstrating the correlation between increasing gain and decreasing gain-peak wavelengths.

2.4. Intracellular InP Nanolasers In Vitro

To enhance material and wavelength stability, we coated InP particles with silica using a modified Stöber method. **Figure 4a** shows a transmission electron micrograph (TEM) of an InP particle coated with a 20-nm thick silica layer. FDTD simulations indicate the resonance wavelength of uncoated microdisks shifts by 7.3 nm when the surrounding refractive index changes by 0.1. The 20-nm silica coating reduces its sensitivity to 0.6 nm. We also produced LPs with thicker (100 nm) silica coatings to further enhance their stability against environmental changes. To facilitate cellular uptake, we further coated the silica-coated InP particles with polyethylene imine (PEI). The positively charged polymer branches of PEI facilitate attachment of LPs onto the negatively charged cell plasma membrane.[12,22] For adherent cells, this initial binding facilitates macropinocytotic internalization of LPs into cells.[10] Recent studies with various cell-line and human blood mononuclear cells have shown the biocompatibility of PEI-coated, as well as antibody-coated, LPs.[12,21]

HeLa cancer cells were tagged with PEI-coated LPs by incubating them in a culture well for 24 hours. Figure 4b shows bright-field and PL images of a 560-nm-sized LP (from batch ii) within a cell under nanosecond pumping. Single-mode lasing was observed (Figure 4b), with a threshold fluence of 2.8 mJ cm^{-2} (≈ 10 pJ per pump pulse). Due to the higher refractive index of the cytoplasm (n = 1.36–1.39) than air, lasing was not observed from smaller particles in batch i. The lasing wavelength showed minimal variation (< 0.1 nm) over 1 million pulses at a 10 kHz repetition rate, demonstrating excellent stability of LPs with 100 nm-thick silica coatings within cells (Figure 4c). At repetition rates below a few MHz, the pump intensity and transient heating are expected to cause minimal perturbation on cells. Figure 4d shows two cells, each containing four intracellular LPs. The presence of multiple LPs per cell enables combinatorial spectral barcoding.[10] With a spectral bandwidth of 230 nm and a spectral bin of 1 nm, the potential number of unique optical

barcodes generated by four randomly positioned LPs is theoretically 114 million (230 choose 4). In a CCK-8 assay, LP-tagged HeLa cells exhibited no significant difference in cell viability over 72 hours compared to untagged control cells (Figure 4e). A Live/Dead assay confirmed excellent cell viability across all particle sizes (Figure 4f).

While thick silica coatings are desirable for wavelength stability, thin- or non-silica coatings offer high sensitivity to the surrounding medium for potential sensing applications. Figure 4g demonstrates a proof-of-concept experiment where two non-coated InP particles in 100 µl of water (n = 1.33) on a glass-bottom dish exhibited wavelength shifts upon the sequential addition of 20 µl of ethanol (n = 1.36). The measured mean shifts were of 0.28 nm for device 1, and 0.30 nm for device 2 following the first addition, and 0.22 nm for device 1 and 0.19 nm for device 2 after the second addition, similar to the theoretical shifts of 0.29 and 0.22 nm, respectively, as predicted by FDTD simulations. Statistical analysis of twenty devices showed a mean shift of 0.27 nm with a standard deviation of 0.05 nm, primarily due to variations in the surface conditions of LPs on a glass dish. In another example, cells were exposed to intense ultraviolet (UV) light to induce apoptosis, and the wavelength shifts of three particles were monitored: one attached to the cell membrane and two embedded within the cytoplasm (Figure 4h). The LP outside the cell membrane showed no wavelength changes (cyan curves), while the cytoplasmic LP located near a ruptured region showed a red-shift of 1.14 nm (green curves), attributed to an increase in the surrounding refractive index by 0.016. The third LP, positioned within a cytoplasmic protrusion, exhibited a blue shift of 0.67 nm (blue curves), corresponding to a decrease in the surrounding refractive index by 0.009. These experiments highlight the potential of high-refractive-index semiconductor LPs as refractive-index sensors for both intracellular and extracellular environments, demonstrating their capability for real-time monitoring of dynamic biological processes.

2.5. Pumping and Detection of LPs through Scattering Media

We investigated the excitation and detection of LPs through highly scattering media. An InP particle (from batch ii) was placed on a glass bottom dish, with translucent tape (3 M Magic Tape) attached beneath the dish to simulate scattering media (**Figure 5a**). The dish was positioned on an inverted microscope and illuminated with 765 nm, 70-ps pump pulses at a repetition rate of 2.5 MHz using a 0.6-NA objective lens. The emitted light was imaged onto a silicon electron-magnification charge-coupled device (EM-CCD) camera with a 100 ms exposure time as layers of tape were sequentially added. Figure 5b shows representative CCD images. Before adding the tape layers, the LP emission formed a small spot with ring interference patterns caused by the 170-µm-thick glass substrate. After the first tape layer (80 µm thick) was applied, speckle patterns began to dominate the images. Autocorrelation analysis indicated that spectral narrowing during lasing increased speckle contrast by approximately 5-fold. This trend persisted with additional tape layers, up to 17 layers (1.36 mm). The speckle pattern sizes increased with the square root of the number of tape layers (Figure 5c), characteristic of a photon diffuse regime. Correspondingly, the lasing threshold pump energy rose approximately quadratically with increasing tape thickness (Figure 5d).

We recorded the photoelectron counts of laser peaks using a line-confocal spectrometer EM-CCD camera at pump energies 1.5 times the threshold values for varying numbers of tape layers. The counts exhibited an exponential decrease with a decay coefficient of 42 cm^{-1} (Figure 5e). For comparison, a similar tape experiment was conducted with a 2-µm-sized InGaAsP microdisk lasing at ~1300 nm under 3-ns pump pulses (2 MHz). The NIR-II particle was detectable through only four layers (Figure 5f), primarily due to the lower sensitivity (≈370 photoelectrons per count, 1 ms exposure) of the InGaAs linescan camera used for detection.

Next, the tape was replaced with hydrated chicken breast tissues of two different thickness: 1–2 mm and 1 cm. Lasing of an InP particle was successfully achieved through both tissue samples, and narrowband emission spectra were detected with high signal-to-noise ratios (SNR) (Figure 5g–j). For the 1 cm-thick tissue, the average threshold pump power was less than 10 mW. In comparison, lasing of an InGaAsP microdisk was observed only in the thinner sample and not in the thicker one, primarily due to the lower efficiency of the InGaAs camera (Figure 5k,l).

These results highlight the advantages of narrowband lasing emission for deep-tissue detection. The sub-nanometer linewidth of the laser emission makes it easily distinguishable from broadband noise sources, such as autofluorescence, CCD electrical noise, and the spontaneous emission background of LPs. For example, using a 0.3-nm detection bandwidth captures the entire laser emission, while reducing inherently broadband fluorescence noise (e.g., with a 60-nm bandwidth) by 200-fold. This results in a 23-dB enhancement of SNR compared to non-spectral detection or luminescent particles lacking laser emission.

2.6. Spectral Detection of Intra-Tissue LP Emission

We performed a series of experiments to evaluate the ability to detect InP LPs within biological tissues. 4T1 murine breast cancer cells expressing green fluorescent protein (GFP) were tagged with PEI-coated LPs (from batch ii) at a 1:1 cell-to-LP mixing ratio. Emission spectra from 137 tagged cells on a culture dish were recorded. The tagged cells were then harvested and injected into the mammary fat pad of an anesthetized Balb/c mouse (**Figure 6a**). Confocal fluorescence microscopy (491 nm excitation) at the injection site visualized the GFP-expressing cells. Using nanosecond pumping at 532 nm, laser peaks were detected from the LPs in the injected cells. Figure 6b shows the emission spectra of three representative cells with distinct lasing wavelengths, which matched to three spectra in the dataset recorded in vitro prior to injection (Figure 6b, orange curves). The spectra detected from the fat pad in vivo exhibited slight broadening, attributed to the wider slit width used in the spectrometer to optimize the SNR.

We also injected LP-tagged 4T1 cells into the tail vein of a mouse using a syringe needle (Figure 6c). An optical coherence tomography image of the injection site visualized a blood vessel approximately 200 µm in diameter located ≈800 µm beneath the skin surface (Figure 6c). During slow cell injection, a 0.45 NA objective lens was used to excite and detect LP emission 1 mm

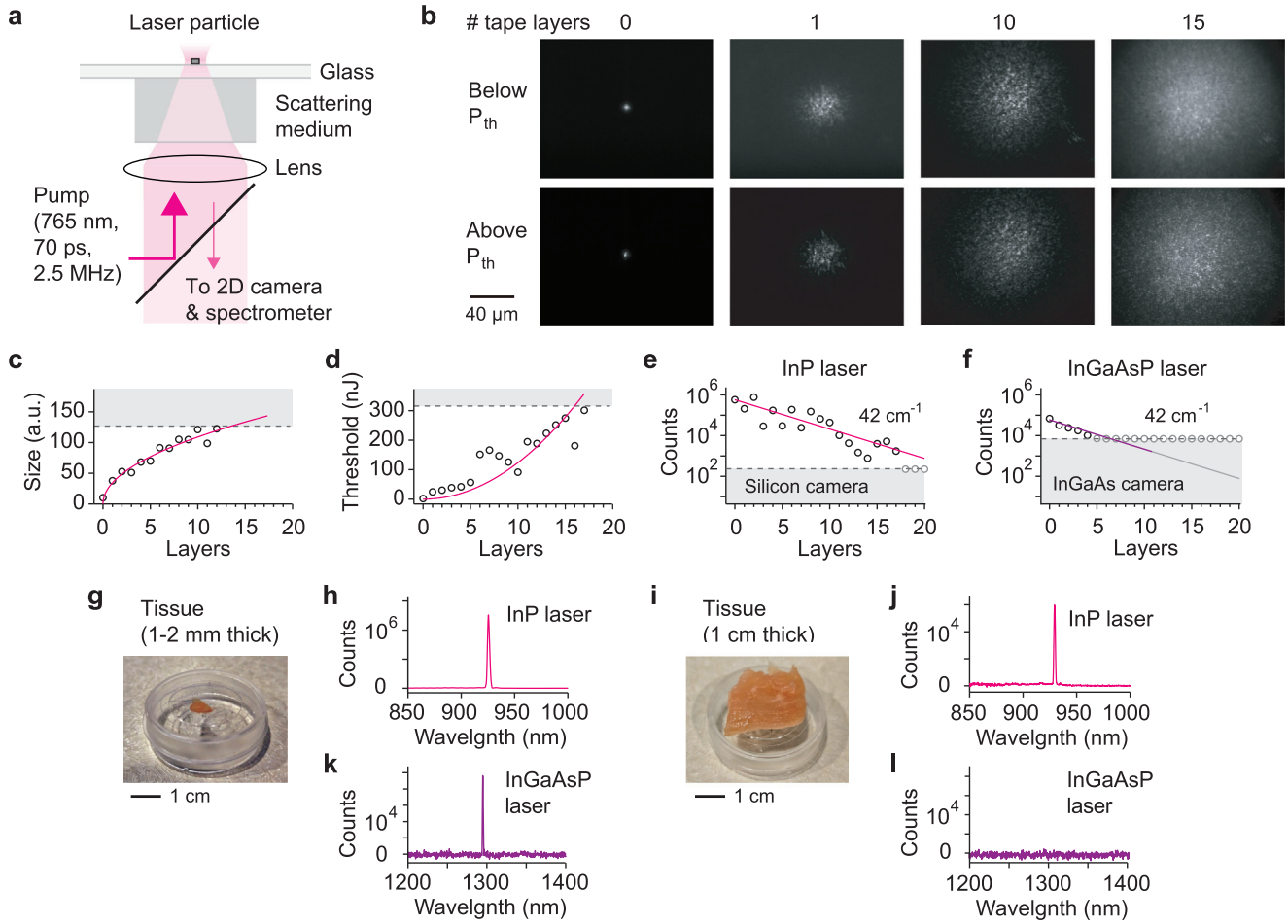

Figure 5. Detection of laser emission through scattering media. a) Schematic of epi-pumping and detection of an LP through scattering media, including tape layers b–f) and chicken breast tissues g–l). (b) Representative widefield images of output emission from a 560-nm-sized InP laser through different numbers of tape layers, shown below and above lasing threshold. (c) Speckle pattern size as a function of tape layer thickness. The dashed line represents the measurement limit imposed by the finite size of the EM-CCD imager. (d) Threshold pump pulse energy required for detecting laser peaks as tape layers are added. The dashed line indicates the maximum energy available from the pump laser. (e) Photoelectron counts of laser peaks from an InP LP. The dashed line indicates the noise floor of the silicon EM-CCD camera in the NIR-I line-confocal spectrometer. (f) Photoelectron counts of laser peaks from an InGaAsP NIR-II LP. The dashed line indicates the noise floor of the InGaAs CCD camera in the NIR-II line-confocal spectrometer. (g) Photograph of a chicken breast tissue slice with a thickness of 1–2 mm. (h) Representative spectrum measured from an InP L through the 1-2-mm thick tissue slice. (i) Photograph of a chicken breast tissue sample with a thickness of 1 cm. (j) Representative spectrum measured from an InP LP through the 1-cm-thick tissue sample. (k) Representative spectrum measured from an InGaAsP NIR-II LP through the thinner tissue sample in (g). (l) Representative spectrum measured from InGaAsP NIR-II LPs through the thicker tissue sample in (i). No laser peaks were detected.

downstream with a pump pulse energy of 1 nJ and a 10 kHz repetition rate. Figure 6d shows spectral density plots acquired at 20 Hz over 16-second period (injection started at 0 s and ended at 11.3 s). Distinct individual spectra persisted for ≈0.2 seconds within the microscope's field of view of 640 μm x 800 μm, suggesting an estimated flow speed of 2–4 mm s^{-1}, consistent with typical tail vein flow velocities.[27] Representative emission spectra recorded at six time points (dashed lines) are shown in Figure 6d.

In a separate experiment, we focused on blood vessels in the mouse ear (Figure 6e). To visualize the ear vasculature before LP imaging, rhodamine-dextran was intravenously injected and imaged using two-photon microscopy (Figure 6e). Subsequently, LP-tagged 4T1 cells were injected into the tail vein, and 532-nm pump pulses were used to excite LPs flowing within the ear vessels. Figure 6f shows a spectrum recorded at location 1 (marked in Figure 6e) and another spectrum recorded 6 minutes later at location 2. Each spectrum persisted approximately 2 seconds within the field of view, corresponding to a flow velocity of 0.32–0.4 mm s^{-1}, consistent with typical micro-venous flow rates.[28]

After the ear imaging, the mouse was euthanized, and internal organs were harvested for further imaging to detect LP signals. Among the detected lasing peaks, 76% were found in the lung, 18% in the liver (Figure 6g), 3% each in the heart and spleen. Figure 6h shows a representative PL image and lasing spectrum obtained from the liver. In another experiment, lasing peaks from LP-tagged cells were excited and detected *ex vivo* through the highly scattering murine skull (Figure 6i) with high SNR (Figure 6j). These results demonstrate the capability of interrogating LPs in deep tissues and identifying their lasing peaks (spectral barcodes) from within biological tissues.

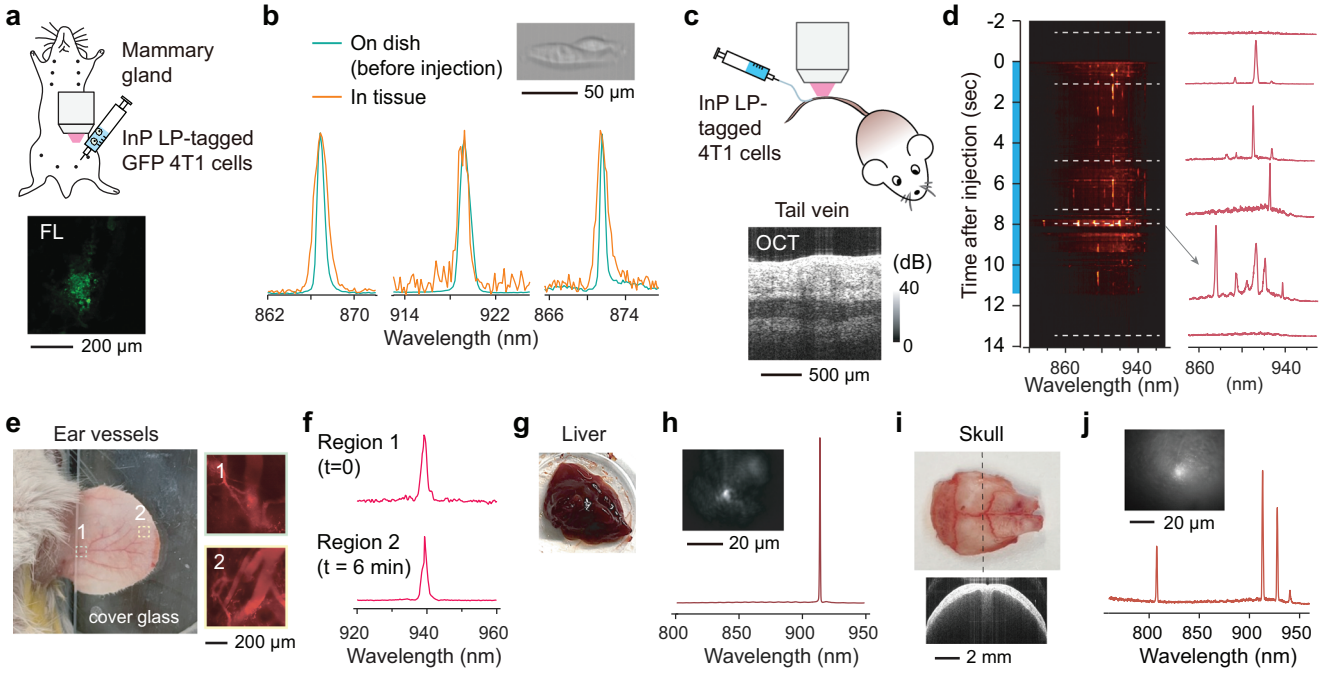

Figure 6. Spectral detection of intra-tissue LP-tagged cells. a) Schematic of LP-tagged GFP-expressing 4T1 cells injected into the mammary fat pad of a mouse. Inset: confocal GFP-fluorescence image of cells at the injection site. b) Emission spectra recorded prior to injection from three cells on a dish plate (green curves; inset: bright-field image) and matching output spectra from the same cells within the fat pad after injection (orange curves). c) Schematic of imaging LP-tagged cells flowing in the tail vein in vivo. Inset: optical coherence tomography (OCT) image of the injection site, located 1 mm upstream of the imaging site. d) Time-lapse spectral density plots recorded from the tail vein during the injection period (blue bar). Representative spectra recorded at six time points (dashed lines; 50 ms exposure each) are displayed on the right. e) Photograph of the murine ear and fluorescence images of vasculature at regions 1 and 2. f) Spectra recorded from an apparently identical cell in region 1 and in region 2 six minutes later. g) Photograph of a liver collected from the mouse after euthanasia. h) Lasing spectrum recorded from the liver tissue. Inset, wide-field PL image. i) Photograph of the murine skull *ex vivo* alongside its OCT image. j) Lasing spectrum from LP-tagged cells excited and detected through the skull. Inset: wide-field PL image of the specimen.

3. Discussion

Using high-gain InP semiconductor material, we have developed submicron-sized LPs that operate within the NIR-I range, expanding the spectral range of semiconductor LPs beyond the previously demonstrated far-red and NIR-II regions. The inherent gain properties of bulk semiconductors, which increase toward shorter wavelengths, enabled ultrawide tuning of the lasing wavelength from 740 nm to 970 nm by varying particle sizes from 1000 to 430 nm. The broad spectral range and nanometer-scale linewidth position InP LPs as promising tools for large-scale barcoding applications.

Notably, batch-i particles in air and batch-ii particles inside cells operated at a WG mode order of 4, the lowest order ever demonstrated for photonic LPs without plasmonic effects. The mode order and laser size may be further reduced by incorporating plasmonic metal coatings to leverage Purcell enhancement and by using shorter pump pulses.[27] For large-scale barcoding applications, mode orders of 6–8 (batches iii-iv) may be more suitable due to their lower thresholds and narrower linewidths than mode orders of 4–5. These sizes were used for in vitro and in vivo experiments in this study. Our simple theoretical model provides accurate estimates of spectral ranges for given particle sizes.

The NIR-I spectral range is particularly advantageous for biological tissue applications. While the longer wavelengths of the NIR-II region benefit from reduced light scattering, the silicon-based detectors compatible with NIR-I are far more cost-effective and exhibit significantly lower electrical noise–1 to 2 orders of magnitude less–than their InGaAs-based counterparts. Compared to visible wavelengths below 700 nm, the NIR-I range of InP LP also avoids spectral overlap with most fluorescent molecules. For example, InP LPs pumped at 765 nm are compatible with most fluorophore-antibody reagents, enabling multiparameter multi-pass flow cytometry.[10]

The narrowband emission from LPs allows for easy distinction from broadband emissions such as fluorescence from NIR dyes and tissue autofluorescence. This ensures that the spectral detection of laser peaks is largely immune to background noise, facilitating deep-tissue detection, as demonstrated with 1 cm-thick chicken tissues. With increasing imaging depth, the threshold pump energy rises due to pump-light diffusion. The measured threshold pump energy was approximately 260 pJ with a 0.45 NA objective lens. The pump intensity at the focal point within tissues is three to five orders of magnitude below typical thresholds for cellular apoptosis and within the maximum permissible exposure limits for tissues.[4] Notably, this is lower than the pulse energy commonly used in multiphoton microscopy and photoacoustic imaging.[29,30] Further studies are needed to evaluate the impact of LP tagging on cellular functions and behaviors in vivo before applying LP-tagged cells in animal models.

In conclusion, InP LPs operating in the NIR-I spectral range offer significant potential for a variety of biological applications, including multi-pass flow cytometry, deep-tissue imaging, and single-cell tracking analysis. Their unique combination of ultrawide tunability, narrowband emission, minimal spectral overlap with widely used fluorophores, and compatibility with cost-effective low-noise silicon detection technologies make them a powerful tool for advanced biomedical research.

4. Experimental Section

InP Particle Fabrication: Custom-designed semiconductor wafers with metal-organic chemical vapor deposition (MOCVD) epitaxial InP/InGaAsP layers on InP substrates were purchased from Seen Semiconductors. Mesa structures were fabricated on the wafers using optical lithography with circular mask patterns ranging in diameter from 900 to 1100 nm, followed by reactive ion etching. To vary the diameters of the InP layers, wafer chips were immersed in hydrochloric (HCl) or hydrophosphoric acid (H_3PO_4) solutions for pre-calibrated etching times. The sacrificial InGaAsP layers were subsequently removed using an acid Piranha solution (H_2SO_4:H_2O_2:H_2O = 1:1:10), releasing the InP particles. Harvested InP particles were washed with ethanol and water and then dispersed in ethanol. For silica (SiO_2) surface coating, a modified Stöber method was used.[10] Nanodisks were suspended in 670 µl of an 80% ethanol solution (v/v). Subsequently, 60 µl of 40 mM tetraethyl orthosilicate (TEOS) in ethanol and 45 µl of 28% ammonium hydroxide (NH_4OH) were added to the suspension. The mixture was then shaken vigorously at 1000 rpm overnight at 70 °C. After the reaction, the coated nanodisks were washed multiple times with water and ethanol. Structural verification of the silica-coated InP particles was performed using a transmission electron microscope (JEOL, JEM 1011) at a magnification of 1:250 000.

Optical Characterizations: Optical experiments were conducted using a home-built hyperspectral microscope system. Two pump sources were employed: a frequency-doubled Nd-YAG laser at 532 nm with a repetition rate of 10 kHz and a pulse duration of 2–4 ns, and an amplified frequency-doubled fiber laser emitting at 765 nm with a repetition rate of 2.5 MHz and a pulse duration of 70 ps. The system utilized either a 0.6 NA, 50x air objective lens or a 0.4 NA, 20x air objective lens. Emission from the sample, collected by the objective lens, passed through a dichroic mirror and a dichroic filter before being split into two paths. One path was directed to a silicon-based EMCCD camera (Luca, Andor) for wide-field imaging. The other path was directed to an EMCCD (Shamrock, Andor) in a spectrometer equipped with two gratings: Grating 1 (300 lines/mm, 500 nm blaze) with a 100 µm slit (resolution: 0.7–0.9 nm) and Grating 2 (1200 lines/mm, 500 nm blaze) with a 100 µm slit (resolution: 0.13 nm). The second output port of the spectrometer was coupled with an avalanche photodiode (APD) and a time-correlated single photon counting (TCSPC) system (Timeharp 260, PicoQuant) to perform transient lifetime spectroscopy. The instrument response function, characterized by using a picosecond pump laser, exhibited a time resolution of 120 ps.

Numerical Simulation: Finite difference time domain (FDTD) simulations were performed using commercial software (Lumerical). Mie scattering simulation employed a total-field scattered-field plane-wave source, while dipole simulations utilized both electric and magnetic dipoles placed inside semiconductor particles. Time-dependent electric and magnetic fields were recorded using densely positioned point-like time monitors within the semiconductor particles. Resonance frequencies (ω_{res}) and the full-width-half-maximum spectral widths ($\Delta\varpi_{res}$) were used to calculate the quality factors (Q) of low-Q modes: $Q = \omega_{res} / \Delta\omega_{res}$. For high Q modes that did not decay completely within the simulation timeframe, Q values were determined from the slope of the electric field decay profiles. 3D near-field field patterns were obtained using an array of 2D field monitors, while far-field emission patterns were calculated using a box monitor that encompassed the particle.

Cell Tagging: HeLa human cervical cancer cells and GFP-4T1 mouse mammary tumor cells were purchased from ATCC (American Type Culture Collection). HeLa cells were cultured in Dulbecco's Modified Eagle Medium (DMEM) supplemented with 10% (v/v) fetal bovine serum (FBS) and 1% (v/v) antibiotic-antimycotic at 37 °C under 5% CO_2. GFP-4T1 cells were cultured in Roswell Park Memorial Institute (RPMI) 1640 supplemented with 10% FBS and 1% antibiotic-antimycotic. For cell tagging experiments, InP particles were further coated with polyethyleneimine (PEI) on top of the silica layer to facilitate cell uptake. For PEI coating, silica-coated InP particles were incubated in a 1:10 volume mixture of PEI solution (50 wt.% in H_2O) and ethanol for 12 hours at room temperature while shaking at 1000 rpm. Particles were thoroughly washed multiple times with water to remove any unbound PEI. Hela or GFP-4T1 cells were first cultured for 24 hours and then co-cultured with PEI-coated particles for an additional 24 hours before further imaging or analysis. For biocompatibility tests, HeLa cells were seeded in 96-well plates with a density of 3000 cells/well and cultured for 24 hours. PEI-coated InP particles with a mean diameter of 730 nm (approximately 1 million particles per ml in cell media) were then added to each well at a density of 6000 particles/well and cultured with the cells for 24, 48, and 72 hours. At each time point, cell viability was assessed using the cell counting kit (CCK8) assay by measuring absorbance (OD) at 450 nm. Cells cultured without particles were used as controls. Live/Dead assays were performed after 72 hours of culture with InP particles from different batches.

Ex Vivo Tissue Experiments: 4T1 cells were tagged with InP LPs from batch ii and cultured on a glass-bottom dish. Chicken breast tissues were sliced into 1~2 mm or 1 cm sections and placed on top of sparsely distributed LPs (batch ii) on a glass substrate. Skull tissue was harvested from a murine carcass and attached to the bottom of a glass dish. For imaging InGaAsP NIR-II LPs, a laser-scanning confocal microscope (Olympus FV3000) was modified to incorporate a nanosecond pump laser at 1064 nm (Spectra Physics VGEN-ISP-POD, pulse duration 3 ns, repetition rate 2 MHz) and a NIR-II spectrometer equipped with an InGaAs linescan camera (Sensor Unlimited 2048). A NIR-optimized 20x, 0.45-NA objective lens (Olympus IMS LCPLN20XIR) was used for imaging.

In Vivo Mouse Experiments: BALB/c mice (female, 10 weeks, 20–25 g) were purchased from Jackson Laboratory. Mice were anesthetized using an intraperitoneal injection of ketamine and xylazine. For fat pad imaging, the skin hair around the mammary gland was removed. GFP-4T1 cells tagged with InP LPs (batch ii) were injected approximately 2 mm away from the nipples to target the underlying fat pad, at an injection depth of ≈3 mm from the tissue surface. Images of injected InP-tagged cells in the fat pad were acquired immediately after injection. For tail vein injection, LP-tagged GFP-4T1 cells suspended in PBS (2000–5000 cells/50 µl) were injected using a cannula. Optical coherence tomography (OCT) imaging was performed using a custom-built system equipped with a swept laser with a center wavelength of 1310 nm. To visualize ear vasculature, a two-photon microscope (Olympus FV4000MPE) was used in conjunction with rhodamine-dextran (2000000 MW, Invitrogen), which was intravenously injected into the tail vein. All animal studies were approved by the Institutional Animal Care and Use Committee (IACUC) of Massachusetts General Brigham and conducted in accordance with National Institutes of Health guidelines (protocol 2017N000021).

Statistical Analysis: Statistical analysis was performed for the data presented in Figures 3 and 4. Data were expressed as mean ± standard deviation (SD). No data transformation or normalization was applied. One-way analysis of variance (ANOVA) was used to assess statistically significant differences between groups. Unpaired Welch's t-tests were performed for pairwise comparisons, with p-values adjusted using the Holm-Sidak method to correct for multiple comparisons. A significance level of $p < 0.05$ was considered statistically significant. All statistical analyses were conducted using GraphPad Prism (GraphPad Software).

Supporting Information

Supporting Information is available from the Wiley Online Library or from the author.

Acknowledgements

S.C. and W.M. contributed equally to this work. This study was supported by National Institutes of Health research grants (R01-EB033155, R01-EB034687). This research used the resources of the Center for Nanoscale Systems, part of Harvard University, a member of the National Nanotechnology Coordinated Infrastructure, supported by the National Science Foundation under award number 1541959.

Conflict of Interest

N.M. and S.H.Y. have financial interests in LASE Innovation Inc., a company focused on commercializing technologies based on laser particles. The financial interests of N.M. and S.H.Y. were reviewed and are managed by Mass General Brigham in accordance with their conflict-of-interest policies. S.C. and W.M. declare no conflict of interest.

Data Availability Statement

The data that support the findings of this study are available from the corresponding author upon reasonable request.

Keywords

III/V semiconductor, deep tissue, in vivo imaging, nanolaser, single cell study

Received: November 29, 2024
Revised: April 18, 2025
Published online:

[1] J. V. Frangioni, *Curr. Opin. Chem. Biol.* **2003**, *7*, 626.
[2] S. A. Hilderbrand, R. Weissleder, *Curr. Opin. Chem. Biol.* **2010**, *14*, 71.
[3] Y. Chen, S. Wang, F. Zhang, *Nat. Rev. Bioeng.* **2023**, *1*, 60.
[4] S. H. Yun, S. J. J. Kwok, *Nat. Biomed. Eng.* **2017**, *1*, 8.
[5] M. E. Matlashov, D. M. Shcherbakova, J. Alvelid, M. Baloban, F. Pennacchietti, A. A. Shemetov, I. Testa, V. V. Verkhusha, *Nat. Commun.* **2020**, *11*, 239.
[6] P. W. Barone, S. Baik, D. A. Heller, M. S. Strano, *Nat. Mater.* **2005**, *4*, 86.
[7] O. T. Bruns, T. S. Bischof, D. K. Harris, D. Franke, Y. Shi, L. Riedemann, A. Bartelt, F. B. Jaworski, J. A. Carr, C. J. Rowlands, *Nat. Biomed. Eng.* **2017**, *1*, 56.
[8] H. Li, X. Wang, T. Y. Ohulchanskyy, G. Chen, *Adv. Mater.* **2021**, *33*, 2000678.
[9] G. Hong, A. L. Antaris, H. Dai, *Nat. Biomed. Eng.* **2017**, *1*, 10.
[10] N. Martino, S. J. J. Kwok, A. C. Liapis, S. Forward, H. Jang, H.-M. Kim, S. J. Wu, J. Wu, P. H. Dannenberg, S.-J. Jang, Y.-H. Lee, S.-H. Yun, *Nat Photon.* **2019**, *13*, 720.
[11] A. H. Fikouras, M. Schubert, M. Karl, J. D. Kumar, S. J. Powis, A. Di Falco, M. C. Gather, *Nat. Commun.* **2018**, *9*, 4817.
[12] S. J. J. Kwok, S. Forward, M. D. Fahlberg, E. R. Assita, S. Cosgriff, S. H. Lee, G. R. Abbott, H. Zhu, N. H. Minasian, A. S. Vote, N. Martino, S.-H. Yun, *Nat. Biomed. Eng.* **2024**, *8*, 310.
[13] D. Sarkar, S. Cho, H. Yan, N. Martino, P. H. Dannenberg, S. H. Yun, *ACS Nano* **2023**, *17*, 16048.
[14] S. Cho, N. Martino, S.-H. Yun, *Nat. Nanotechnol* **2025**, *20*, 404.
[15] M. Schubert, L. Woolfson, I. R. M. Barnard, A. M. Dorward, B. Casement, A. Morton, G. B. Robertson, P. L. Appleton, G. B. Miles, C. S. Tucker, *Nat. Photonics* **2020**, *14*, 452.
[16] A. Kavčič, M. Garvas, M. Marinčič, K. Unger, A. M. Coclite, B. Majaron, M. Humar, *Nat. Commun.* **2022**, *13*, 1269.
[17] Z. Wang, B. Tian, M. Paladugu, M. Pantouvaki, N. Le Thomas, C. Merckling, W. Guo, J. Dekoster, J. Van Campenhout, P. Absil, *Nano Lett.* **2013**, *13*, 5063.
[18] I. Vurgaftman, J. Á. R. Meyer, L. R. Ram-Mohan, *J. Appl. Phys.* **2001**, *89*, 5815.
[19] H. J. Joyce, C. J. Docherty, Q. Gao, H. H. Tan, C. Jagadish, J. Lloyd-Hughes, L. M. Herz, M. B. Johnston, *Nanotechnology* **2013**, *24*, 214006.
[20] R. J. Hussey, G. I. Sproule, J. P. McCaffrey, M. J. Graham, *Oxidat. Metals* **2002**, *57*, 427.
[21] N. Martino, H. Yan, G. Abbott, M. Fahlberg, S. Forward, K.-H. Kim, Y. Wu, H. Zhu, S. J. J. Kwok, S.-H. Yun, *Light Sci. Appl.* **2025**, *14*, 148.
[22] M. Schubert, K. Volckaert, M. Karl, A. Morton, P. Liehm, G. B. Miles, S. J. Powis, M. C. Gather, *Sci. Rep.* **2017**, *7*, 40877.
[23] N. Matine, M. W. Dvorak, J. L. Pelouard, F. Pardo, C. R. Bolognesi, presented at *Conference Proceedings. 1998 International Conference on Indium Phosphide and Related Materials (Cat. No. 98CH36129)*, IEEE, **1998**, pp. 195–198.
[24] S. L. Chuang, J. O'Gorman, A. F. J. Levi, *IEEE J. Quantum Electron* **1993**, *29*, 1631.
[25] O. Svelto, D. C. Hanna, in *Principles of Lasers*, Springer, Berlin **2010**.
[26] R. H. Yan, S. W. Corzine, L. A. Coldren, I. Suemune, *IEEE J. Quantum Electron.* **1990**, *26*, 213.
[27] Y. Hu, W. Tang, P. Cheng, Q. Zhou, X. Tian, X. Wei, H. He, *Cytometry, Part A* **2019**, *95*, 657.
[28] Y. Zhou, J. Liang, K. I. Maslov, L. V. Wang, *Opt. Lett.* **2013**, *38*, 3882.
[29] J. Park, S. Choi, F. Knieling, B. Clingman, S. Bohndiek, L. V. Wang, C. Kim, *Nat. Rev. Bioeng.* **2025**, *3*, 193.
[30] C. Xu, M. Nedergaard, D. J. Fowell, P. Friedl, N. Ji, *Cell* **2024**, *187*, 4458.

Supporting Information

Wideband Tuning and Deep-Tissue Spectral Detection of Indium Phosphide Nano-Laser Particles

Sangyeon Cho[1], Wonjoon Moon[1], Nicola Martino[1], Seok Hyun Yun[1,2]*

[1] Harvard Medical School and Wellman Center for Photomedicine, Massachusetts General Hospital, Cambridge, Massachusetts, 02139, USA

[2] Harvard-MIT Health Sciences and Technology, Massachusetts Institute of Technology, Cambridge, Massachusetts, 02139, USA

*E-mail: syun@hms.harvard.edu

Supplementary Note 1: Whispering Gallery Mode (WGM) Model

For large disks with radius R much greater than the free-space optical wavelength λ, the electric field profile of the fundamental radial WGM with the m-th azimuthal order is approximated by the Bessel function of the first kind of order m, with the first node located at the edge of the disk [1]. For large mode order m, the resonance wavelength is given by:

$$\lambda_m = \frac{2\pi n_m R}{x_m} \qquad (1)$$

where n_m is the effective refractive index of the mode, and x_m is the first zero of the Bessel function of order m. The value of n_m typically varies with wavelength and is lower than the refractive index of the disk material due to the presence of the electric field in the surrounding medium (air) above and below the disk surfaces.

The parameter $x_m$can be approximated as a linear function of m:

$$x_m = a_m\, m + b_m \qquad (2)$$

where $a_m = x_{m+1} - x_m$ and $b_m = x_m - a_m m$. For example, for mode order m ranging from 2 to 15, the values are approximately $a_m \approx 1.14$ and $b_m \approx 3.01$ (see Fig. S1).

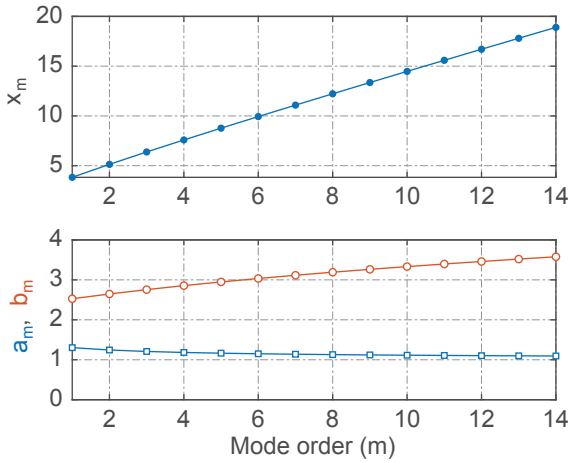

Figure S1. Bessel zeros (top) and a_m, b_m as a function of mode order

We can express the resonance wavelength as:

$$\lambda_m = \frac{2\pi n_m R}{a_m m + b_m} \qquad (3)$$

In terms of photon energy,

$$E_m = \frac{hca_m}{2\pi n_m R}\left(m + \frac{b_m}{a_m}\right) \qquad (4)$$

where h is Planck's constant and c is the speed of light. Since n_m, a_m, and b_m vary slowly with mode order, the free spectral range (FSR) in energy, $\Delta E_{FSR,m}$, is approximately:

$$\Delta E_{FSR,m} \equiv E_{m+1} - E_m \approx \frac{hca_m}{2\pi n_m R} \qquad (5)$$

Thus, the photon energy can be rewritten as:

$$E_m = \Delta E_{FSR,m}\left(m + \frac{b_m}{a_m}\right) \qquad (6)$$

For small disks, with sizes comparable to the optical wavelength (and therefore low mode orders), the mode field profile extends beyond the disk edge. As a result, Eq. (1) underestimate λ_m.

To account for this, we treat n_m/a_m as an effective constant and use the same functional form as Eq. (3) to write a simplified model:

$$\lambda_m = \frac{2\pi nR}{(m + b/a)} \qquad (7)$$

Here, $n = n_m/a_m$ is an effective refractive index, and a (equal to a_m) and b (less than b_m) are constant parameters. In this study, we chose to use a = 1.14 and $b/a \equiv m_0 = \pi/2$ (i.e., b = 1.79).

Figure S2 shows resonance wavelengths computed by solving Maxwell's equations using a full electromagnetic model[2] for InP disks (material refractive index of 3.5), for mode orders between 3 and 10 in the spectral range of 700-1000 nm. Equation (7), using n_m = 3 and $b/a = \pi/2$, matches the numerical dispersion curves reasonably well (see Fig. S2).

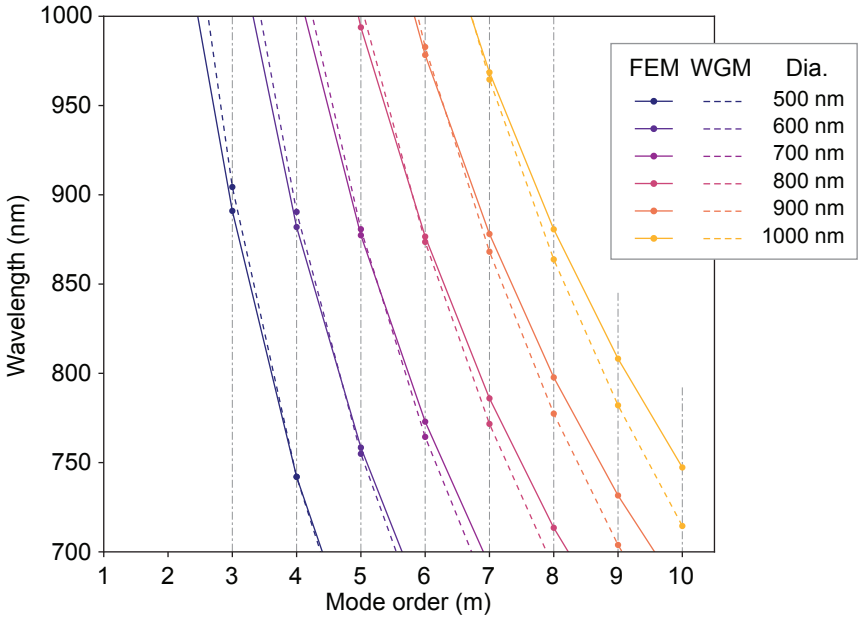

Figure S2. Resonance wavelengths of different WGM mode orders for disks with diameters ranging from 500 nm to 1000 nm. Solid curves represent numerical results by solving the finite-element method. Dashed curves show the simplified analytic model based on Eq. (7), using n_m = 3, a_m = 1.14, and thus an effective refractive index n = 2.6.

Interpretation of the model in Eq. (7) from a geometric optics perspective

Rearranging Eq. (7), we obtain

$$m = \frac{2\pi nR}{\lambda_m} - m_0 \quad (8)$$

Let $L \equiv 2\pi R_{eff}$ represent the effective propagation pathlength of the WGM within the disk, where R_{eff} is the effective radius of the WGM trajectory.

From a geometrical optics perspective, the mode order corresponds to the number of wavelengths that fit along the roundtrip path within the cavity:

$$m = \frac{nL}{\lambda_m} \quad (9)$$

Using the same effective index n as in Eq. (7), and comparing Eqs. (8) and (9), we find:

$$L = 2\pi R - m_0 \frac{\lambda_m}{n} \quad (10)$$

$$R_{eff} = R - \frac{m_0}{2\pi}\frac{\lambda_m}{n} \quad (11)$$

Therefore, the difference Δ between the physical and effective radii of the WGM is:

$$\Delta = \frac{m_0}{2\pi}\frac{\lambda_m}{n} \quad (12)$$

In our simulation, we used $m_0 = \frac{\pi}{4}$ yielding,

$$\Delta = \frac{1}{8}\frac{\lambda_m}{n} \quad (13)$$

References

1. N.C. Frateschi, A.F.J. Levi. The spectrum of microdisk lasers. Journal of Applied Physics 1996, 80, 644.
2. J. E. Heebner, T. C. Bond, J. S. Kallman. Generalized formulation for performance degradations due to bending and edge scattering loss in microdisk resonators. Optics Express 2007, 15, 4452.

Table S1. Representative room-temperature NIR-I micro- and nano-lasers to date.

	Gain material (Lattice matching)	Wavelength	Device size (Shape)	Threshold pump (Calculated)	Pulse /Duration (Repetition)	Environmental stability	Year [Ref]
1	GaAs/AlGaAs/ GaAs (GaAs)	840 nm	Length: 6 μm Thickness: 430 nm (Nanowire)	202 μJ/cm^2 (505 MW/cm^2)	522 nm / 400 fs (20.8 MHz)	Stable in air, Likely stable in water	2013 [1]
2	InP (Silicon)	880 nm	Length: ~ few μm Thickness: 430 nm (Nanowire)	1.69 pJ (34 MW/cm^2)	532 nm / 7 ns (321 Hz)	Stable in air, Likely stable in water	2013 [2]
3	$CH_3NH3PbI_3$	787 nm	Length: 8.5 μm Thickness: 500 nm (Nanowire)	0.6 μJ/cm^2 (6 MW/cm^2)	402 nm / 100 fs (250 kHz)	Quickly dissolve in water	2015 [3]
4	GaAsSb-superlattice (GaAs)	950 nm	Length: 10 μm Thickness: 440 nm (Nanowire)	6 kW/cm^2	800 nm / 150 fs (80 MHz)	Stable in air, Likely stable in water	2018 [4]
5	InGaAs/GaAs quantum well	950 nm	Length: 2.2 μm Thickness: 200 nm (Nanowire)	0.48 μJ/cm^2 (13.7 MW/cm^2)	800 nm / 35 fs (85 MHz)	Stable in air, Likely stable in water	2021 [5]
6	InP	740-870 nm	Length: 480 nm Thickness: 300 nm (Cube)	3.5 mJ/cm^2 (0.7 MW/cm^2)	532 nm / 5 ns (10 kHz)	Stable in air and water	This work
6	InP	840-950 nm	Dia.: 730 nm Thickness: 300 nm (Disc)	0.2 mJ/cm^2 (0.04 MW/cm^2)	532 nm / 5 ns (10 kHz)	Stable in air and water	This work

[1] D. Saxena, S. Mokkapati, P. Parkinson, N. Jiang, Q. Gao, H. H. Tan, C. Jagadish, Nat Photonics 2013, 7, 963.

[2] Z. Wang, B. Tian, M. Paladugu, M. Pantouvaki, N. Le Thomas, C. Merckling, W. Guo, J. Dekoster, J. Van Campenhout, P. Absil, Nano Lett 2013, 13, 5063.

[3] H. Zhu, Y. Fu, F. Meng, X. Wu, Z. Gong, Q. Ding, M. V Gustafsson, M. T. Trinh, S. Jin, X. Y. Zhu, Nat Mater 2015, 14, 636.

[4] D. Ren, L. Ahtapodov, J. S. Nilsen, J. Yang, A. Gustafsson, J. Huh, G. J. Conibeer, A. T. J. Van Helvoort, B.-O. Fimland, H. Weman, Nano Lett 2018, 18, 2304.

[5] X. Zhang, R. Yi, N. Gagrani, Z. Li, F. Zhang, X. Gan, X. Yao, X. Yuan, N. Wang, J. Zhao, ACS Nano 2021, 15, 9126.